



EFFECTS OF PIN FIN SHAPE AND SIZE ON TURBINE BLADE TRAILING EDGE FLOW AND HEAT TRANSFER

Tuğba TUNÇEL* and Harika S. KAHVECİ**

Aerospace Engineering Department, Middle East Technical University (METU), 06800, Ankara, Turkey

*ttuncel@metu.edu.tr, **kahveci@metu.edu.tr (corresponding author)

(Geliş Tarihi: 19.01.2019, Kabul Tarihi: 17.08.2019)

Abstract: In modern turbine blades, pressure-side cutbacks with film-cooling slots stiffened with lands and pin fins that are embedded in passages are used to cool trailing edges. There are many studies that have investigated these cooling configurations from a thermal perspective, while only a limited number have been concerned with the aerodynamic aspects. This study presents a thorough computational investigation of a film-cooling configuration to determine the optimum combination of shape and size of pin arrays. The analyses are performed to include both internal and external surfaces of the trailing-edge cutback region and the results are evaluated from both aerodynamics and thermal aspects. The internal structure of the configuration studied consists of staggered arrays of pins and airfoil-shaped blockages in front of the slot exits that open into a pressure-side cutback region. The pins used are of circular, elliptical, or airfoil shapes that are rarely studied in such configurations, and of different sizes, resulting in five different models for comparisons. The flow features, pressure losses and heat transfer characteristics inside of the trailing-edge surfaces and in the vicinity of the slots and on the external cutback region are examined. The airfoil-shaped pins are found to decrease the pressure losses in internal flow compared to the other pin shapes of similar size. However, the pin arrays produce minor differences in the velocity contours in the breakout region, resulting in similar pressure loss trends here. The small-sized pins are found to demonstrate slightly higher film-cooling effectiveness on the breakout surface due to lower temperatures at the slot exit. It can be inferred from the results that, since the airfoil-shaped pin reduces the aerodynamic penalty across the internal pin array, performing an optimization on the size of these pins to achieve the desired cooling performance could be a reasonable approach in the design process.

Keywords: Turbine, trailing edge, film cooling, pressure loss, heat transfer coefficient, film-cooling effectiveness

PİN FİN ŞEKLİ VE BÜYÜKLÜĞÜNÜN TÜRBİN KANADI FIRAR KENARINDAKİ AKIŞ VE ISI TRANSFERİNE ETKİLERİ

Özet: Modern türbin kanatlarının firar kenarlarının soğutulmasında, adalarla desteklenen film soğutması oluklarının bulunduğu kesik basınç kenarları ve soğutma kanallarının içine yerleştirilen pin fin yapıları kullanılmaktadır. Bu soğutma konfigürasyonlarını termal açıdan inceleyen pek çok çalışma olmasına rağmen, aerodinamik açıdan inceleme yapan çalışmalar sınırlı sayıdadır. Bu çalışma bir film soğutması konfigürasyonunun, pin dizini şekil ve büyüklüğünün optimum kombinasyonunu belirlemek için yapılan detaylı bir hesaplamalı incelemesini sunmaktadır. Analizler, firar kenarındaki kesik bölgenin hem iç hem dış yüzeylerini kapsayacak şekilde yapılmış ve sonuçlar hem aerodinamik hem de termal açıdan değerlendirilmiştir. Çalışılan konfigürasyonun iç bölgesi, saptırılmış pin dizinleri ve kesik basınç kenarına açılan olukların önünde bulunan kanat şeklindeki tıkaçıcılardan oluşmaktadır. Çalışmada, dairesel, eliptik ve bu tür konfigürasyonlarda nadir olarak çalışılmış olan kanat şekillerine sahip ve farklı büyüklüklerde olan pinler kullanılmış ve karşılaştırmalar için beş farklı model oluşturulmuştur. Firar kenarı yüzeylerinde, olukların civarında ve kesik dış yüzey bölgesindeki akış özellikleri, basınç kayıpları ve ısı transferi karakteristiği incelenmiştir. Elde edilen sonuçlar kanat şeklindeki pinlerin aynı büyüklükteki diğer şekilli pinlere göre, iç akışta basınç kayıplarını azalttığını göstermektedir. Bununla birlikte pin dizinleri, firar kenarı ayrışma bölgesindeki hız konturlarında küçük farklar oluşturmakta ve burada benzer basınç kayıplarına sebep olmaktadır. Küçük pinlerin, oluk çıkışlarındaki daha düşük sıcaklık seviyelerinden ötürü, firar kenarı ayrışma yüzeyinde biraz daha yüksek film soğutması verimliliği sağladığı görülmüştür. Sonuç olarak, kanat şeklindeki pinler kanat içindeki dizinde aerodinamik kayıpları azalttığı için, hedeflenen soğutma performansını elde etmek üzere bu pin şeklinin boyut optimizasyonunun yapılması tasarım aşamasında uygun bir yaklaşım olacaktır.

Anahtar Kelimeler: Türbin, firar kenarı, film soğutması, basınç kaybı, ısı transferi katsayısı, film soğutması verimliliği

NOMENCLATURE

D	Pin diameter [mm]
H	Channel height [mm]
H_p	Pin height [mm]
h	Convection heat transfer coefficient [W/m ² K]
k	Thermal conductivity [W/mK]
L	Total streamwise length of trailing-edge [mm]
Nu	Nusselt number [= hD/k_f]
P	Static pressure [kPa]
P_T	Upstream total pressure [kPa]
S_p	Streamwise distance between pins [mm]
q''	Wall heat flux [W/m ²]
s	Entropy [J/kg.K]
T	Temperature [K]
u	Velocity [m/s]
u_s'	Non-dimensional velocity [= u_s/u_{bulk}]
X_p	Lateral distance between pins [mm]
X	Axial distance from slot exit [mm]
x	Axial coordinate
ρ	Density [kg/m ³]
ψ	Total pressure coefficient [= $(P_T - P_{T,i})/(\rho_i u_i^2/2)$]
ω	Vorticity [s ⁻¹]
ω'	Non-dimensional vorticity [= $\omega_s H/u_i$]

Subscripts

e	Exit
f	Fluid
i	Inlet
l	Local value
s	Streamwise
∞	Mainstream
up	Upstream

INTRODUCTION

It is known that the thermal efficiency of gas turbines strongly depends on the turbine entry temperature of the working fluid. With improved turbine designs, peak temperatures in advanced gas turbines, especially those used for aerospace propulsion, have been around 2000 K or even more for quite some time, and these levels are well above the maximum allowable metal temperature (Han et al., 2013). To overcome material temperature limits, internal and external cooling techniques have been developed and extensively used for turbine blades.

Due to structural and aerodynamic restrictions, enhancing trailing edge cooling methods creates a challenge for designers. To overcome this challenge a frequently used method is cutting out the pressure side of the trailing edge to form span-wise coolant ejection slots. From these slots, coolant is ejected through the cutback region creating a film of lower-temperature gas, which protects the trailing edge from the mainstream hot gas. This type of cooling in the trailing edge region is generally used together with pin fins or ribs placed inside of coolant channels. Those structures are used both to increase convective heat transfer by augmenting turbulence levels and to assure structural integrity.

Coolant channel structures, especially circular pin fins, were studied in great detail in literature since they are being used in many other cooling applications as well. An early study done by Brigham and VanFossen (1984) focused on the pin length-to-diameter ratio and found that this ratio has a major effect on heat transfer coefficient. Further, they showed that when this ratio is below 2, Nusselt number depends on the Reynolds number, but not on the length-to-diameter ratio anymore. Metzger et al. (1986) performed experiments to investigate the heat transfer performance of arbitrary combinations of circular pins by changing the diameter and the streamwise spacing of pins in constant and converging flow areas, separately. Then, they used a superimposition technique to obtain the Nusselt number for complex combinations of circular pin-fin arrays. Armstrong and Winstanley (1988) performed a review on the turbine cooling applications using a staggered-array of pin fins. Their findings showed that the research results on pin-fin heat transfer and flow friction were not enough to develop generalized heat-transfer and friction-loss correlations. An experimental investigation for heat transfer capabilities of partial-length circular pin fins was performed by Arora and Abdel-Messeh (1990). As a result of these experiments, it was found that both heat transfer and pressure loss are inversely proportional to the pin-tip clearance. Ligrani and Mahmood (2003) focused on the effects of the coolant-to-wall temperature ratio on the Nusselt number and friction factor. They concluded that as this ratio decreased, the Nusselt number increased while the friction factor decreased. Chyu (1990) compared circular pins with and without endwall fillet radius and discovered that the pins without the endwall fillet caused higher heat transfer and lower pressure loss.

Although circular pins are the most frequently used turbulence promoters due to their easy manufacturing, to further increase heat transfer, the effects of different pin shapes have been investigated by different researchers. A major study on effects of pin shape on pressure loss and heat transfer was conducted by Metzger et al. (1984). In this work, experiments were performed for two families of array geometries. Pressure loss and heat transfer coefficients of oblong-shaped pins and circular pins were compared. It was found that although heat transfer performance of oblong-shaped pins are 20% higher than that of circular pins, the resulting pressure loss is 100% higher, which is a noticeable disadvantage to the use of such pins at regions where a trade-off exists between heat transfer and aerodynamics. In addition, they studied the arrangement of circular pin fins and found that changing it from inline to staggered configuration not only increased the heat transfer, but also decreased the pressure loss at the same time.

Chyu et al. (1998) conducted experiments with cubic and diamond-shaped pins. Since they result in a high heat transfer enhancement while maintaining a moderate pressure penalty, cubic pins can be used as an alternative to circular pins. A similar comparison between elliptical and circular pins was done by Li et al. (1998). Elliptical

pins had a major-to-minor axis ratio of 1.78 and the same circumference with that of the circular pins. Heat transfer and resistance coefficients of both pin shapes were calculated using experimental measurements. It was found that for the investigated range of Reynolds numbers between 1000 to 10000, elliptical pins display both higher convective heat transfer performance and less flow resistance.

In another study, Uzol and Camci (2005) used elliptical pins having the same frontal area with that of circular pins, rather than the circumference. They investigated the reasons for the improved aerodynamic performance of elliptical pins. Studying the flow structures around pins, they concluded that the wake of circular pins are higher than those of elliptical pins which enhance heat transfer but create higher pressure loss.

Chen et al. (1997) proposed drop-shaped pins as an alternative to circular pins. In their research, naphthalene sublimation technique was used to investigate the flow field. The results showed that depending on their relative spacings, drop-shaped pins demonstrate 41% to 52% less flow resistance with increased overall heat transfer performance in the studied Reynolds number range.

More recently, Ling et al. (2013) measured the three-dimensional velocity and concentration fields of the flow through the pressure-side cutback region of a NACA-0012 airfoil, with a plenum located inside of the airfoil consisting of an array of four rows of staggered pin fins. The study focused on the flow characteristics at the slot exit and on the breakout surface. Comparisons between two trailing-edge configurations, one with thin straight lands and airfoil-shaped blockages and one without, revealed that the thinner lands of the former airfoil resulted in higher spanwise average surface effectiveness, but in lower coolant concentration uniformity.

In a subsequent study, Ling et al. (2015) performed RANS modeling of the same trailing-edge slot configuration with and without blockages. They showed that the $k-\omega$ SST turbulence model under-predicts the turbulent viscosity both throughout the pin-fin array and on the breakout surface resulting in inaccurate velocity calculations and coolant concentration. Likewise, Ames and Dvorak (2006) performed experiments searching for the reasons behind heat transfer enhancement of pin fins. They modeled their experiments using conventional turbulence models. Their findings suggest that all of the turbulence models they used under-predict both the heat transfer and the pressure drop.

As in Ling et al. (2015) and Ames and Dvorak (2006), there have been other attempts to approach the problem from a numerical standpoint in addition to experimentation. In their study, Martini et al. (2006) modeled three different internal cooling structures using unsteady Detached Eddy Simulation (DES). Their results showed that for examining discharge coefficients, steady RANS models could be used as an alternative to time consuming unsteady DES calculations. Wang et al.

(2012) performed both experiments and computations with five different pin geometries with the same cross-sectional areas. While flow structures showed distinct differences between the data and the predictions, the pressure loss behaviors were found to be in good agreement. Their findings suggest that drop-shaped pins can be used as an alternative to circular pins. More recently, Fernandes et al. (2017) studied the accuracy of the well-known turbulence models in the prediction of heat transfer rates and pressure distribution on the surface of pin fins. They concluded that the quadratic realizable $k-\epsilon$ and the $k-\omega$ SST turbulence models estimate the heat transfer rates the most accurately.

Kacker and Whitelaw (1969) conducted experiments to find a correlation between adiabatic wall effectiveness and slot lip thickness-to-slot height ratio. They concluded that those two parameters are inversely proportional to each other. Sivasegaram and Whitelaw (1969) considered the effects of slot lip thickness-to-slot height ratio and the injection angle on film-cooling effectiveness. Their findings on slot lip thickness-to-slot height ratio agree with the earlier study.

More recently, Horbach et al. (2010) investigated the aerodynamic and heat transfer performance of different lip geometries. This study revealed that the lip thickness affects the mixing of coolant and the main flow at the slot, but the lip shape does not considerably affect the thermal and aerodynamic performance of film cooling. Horbach et al. (2011) used the same setup with three different pin-fin configurations and studied their effects on the external film-cooling performance. The streamwise-oriented pins gave higher discharge coefficients and lower heat-transfer performance, while the spanwise-oriented pins gave lower discharge coefficients and higher heat-transfer performance.

Taslim et al. (1992) investigated the effects of the injection angle, slot lip thickness-to-height ratio, slot width-to-height ratio, blowing ratio, and the coolant-to-mainstream density ratio on film effectiveness. The film effectiveness was found to be insensitive to the density ratio and slot aspect ratios, while lip thickness-to-height ratio and the injection angle had considerable impact on film effectiveness.

There are many studies that investigate the coolant flow through a trailing-edge slot geometry from a thermal performance perspective, while only a limited number of studies have been concerned with the aerodynamic aspects. Among those limited studies, mostly circular pins have been of interest, while studies on other shapes have been much less in number. This study presents a thorough investigation of the effect of the internal pin-array structure on both the internal passage and the downstream trailing edge slot exit flow from both aerodynamic and thermal aspects. Different pin shapes that are of circular, elliptical, and airfoil shape (NACA 0033 profile) with varying sizes are modeled, presenting detailed comparisons. The airfoil shape is rather a more novel shape type that has been studied scarcely. In the

study, the same airfoil shape (NACA 0033) was adopted with that of the island blockage of the trailing edge configuration, resulting in a unique pin-array and blockage combination that has not been investigated before to the authors' knowledge. The results obtained in the internal cooling structure provide the inlet coolant profiles for the external cooling structure that consists of the pressure-side cutback slot region. The goal is to select an optimum pin-fin configuration that is more advantageous for use in blade trailing-edge design.

NUMERICAL PROCEDURE

ANSYS CFX 18.2 (2017) was used as the Computational Fluid Dynamics (CFD) solver for the simulations. The solver uses an element-based finite volume technique to solve the 3D Reynolds-Averaged Navier-Stokes (RANS) equations. A high-resolution advection scheme was used for the evaluation of the discretized equations. The Reynolds stresses are modeled using the $k-\omega$ -based Shear Stress Transport (SST) (Menter et al. 2003) that is a two-equation Eddy Viscosity turbulence model. This model behaves like the $k-\epsilon$ model outside of the boundary layer and the $k-\omega$ model inside of the boundary layer. The automatic wall function provided by CFX automatically switches from a low-Reynolds to a near-wall formulation when the boundary layer is highly resolved (ANSYS Inc., 2017). For meshing, ICM software of the ANSYS CFD package was used.

The study is divided into two parts. In the first part, the aerodynamic and thermal performances of the pin fins inside the internal cooling channel are investigated. In the second part, the investigation has focused on the effects of pin-fin arrays on the flow structure at the slot exit region and the downstream region. The flow conditions generated by different pin arrays at the end of the internal section of the trailing edge were applied at the slot exit as the inlet boundary conditions to the external flow domain of the computations.

Before initiating the comparative study, a configuration for which experimental data exists in literature was modeled and computations were validated. During iterations, mesh sensitivity studies were conducted to ensure proper convergence of the CFD solutions. Later, the comparative study was performed for trailing edge internal structure and external surface with different pin shapes and sizes in order to investigate the losses and heat transfer characteristics of the pin arrays.

Validation of Computational Methodology

The data obtained by Ling et al. (2013) from an airfoil section with the airfoil-shaped blockages in the slots is used for validation. The experiments were performed via Magnetic Resonance Imaging (MRI) technique. The details on the setup used can be found in the referenced paper. Figure 1 demonstrates the full model (a) and the fluid domains used for the analyses of internal (b) and external (c) trailing-edge sections separately. In the first part of the study, the flow inside the internal domain (b)

containing the pin arrays is investigated. In the second part, the flow in the external domain (c) that includes the breakout surface is studied with only the half of the slot and half of the land modeled, considering the symmetry of the geometry.

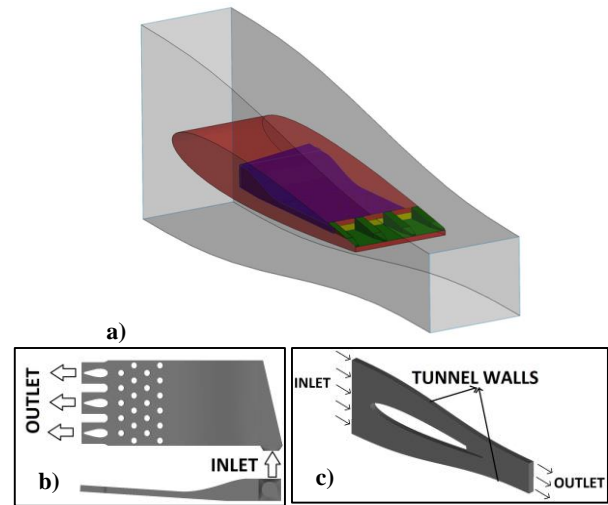


Figure 1. a) Computational model, and fluid domains for b) internal and c) external sections

Simulations for the validation of the current study were performed with this same configuration and for the same experimental conditions given in Tables 1 and 2. There were no measurements of the turbulence performed for these experiments, but a low-free stream intensity was expected based on the inlet conditions and the configuration (Ling et al., 2014). In the current study, the turbulence intensity was assumed to be 5% for the computations. The sensitivity study for the turbulence intensity levels of 1%, 5% and 10% per CFX default settings confirmed that the average variation in local velocity values between the turbulence levels was less than 2%.

Table 1. Experimental conditions from Ling et al. (2013), used for internal domain

Bulk Velocity at Slot Exit	0.39 m/s
Coolant Velocity at Slot Exit	0.30 m/s
Temperature	20 ° C
Working Fluid Density	998 kg/m ³
Coolant Mass Flow Rate	4.41 l/min

In the internal domain of Figure 1-b, the coolant flow enters the domain through the manifold on the side, and moves downstream through the pins, finally leaving the section through the trailing edge slots. In the experiment, the flow was mentioned to be highly non-uniform at the plenum entrance, with no profile information. But it was also observed that the predictions were insensitive to the coolant inlet conditions (Ling et al., 2014). Hence the inlet velocity to the computational domain is taken to be uniform in this study. In Ling et al. (2013), the variation in the volumetric flow rate out of each slot is quoted to be less than 6%, which agreed well with the predictions.

The typical velocity-inlet and static pressure-outlet type of boundary conditions were applied on the model. The inlet velocity is determined through iterations so that the average coolant velocity at the slot exit and the coolant mass flow rate given in Table 1 are matched with that of the experiment. The end walls, pins, slots, and the airfoil-shaped blockages were modeled with no-slip and fixed temperature surfaces. The coolant used in the experiments was water and is modeled at 1atm reference pressure and at 25°C reference temperature with a specific heat capacity of 4181.7 J/kg.K at constant pressure and a dynamic viscosity of 8.899×10^{-4} kg/m.s. Benson et al. (2012) performed experiments at the same test facility at higher Reynolds numbers and concluded that even if the Reynolds number range that was tested with water was significantly less than that in the real engine environment, the flow under those conditions was fully turbulent representing the realistic conditions. Besides, Ling et al. (2014) have stated that the compressibility effects do not affect turbulent mixing at the given experimental conditions.

For meshing, the domain is discretized using unstructured tetrahedral elements and prism elements are used in near-wall regions in order to resolve the boundary layer. A mesh sensitivity study was conducted by using different sizes of three meshes with the number of elements varying from 1.1M to 5.6M. The sensitivity study was performed by monitoring the velocity profiles and total pressure along the centerline of the pin array across the top and bottom walls of the computational domain. The average percentage of differences in velocities between 1.1M and 2.4M was calculated as 11.3% while 2.4M and 5.6M was calculated as 9.1%. It should be noted that the percentages are magnified due to low velocities. In fact, the comparison of total pressure values resulted in a 5.4% of difference between each mesh. Due to the computational cost of further refinement, the mesh with 2.4 M elements was selected for the validation study. The selected mesh was constructed such that 19 prism layers spanned the boundary layer with a first-layer height that ensured $y^+ < 1$ everywhere in the domain. Those conditions were satisfied with 0.006 mm near-wall spacing and 0.93 mm boundary layer thickness. The solution convergence was confirmed when residuals of mass, momentum, and energy equations reached levels of 10^{-6} .

The comparison between the predictions and the experiment is shown in Figure 2 in the form of contours of streamwise velocity component through the pin arrays and the slot exit of the test configuration. The velocity was non-dimensionalized with the average experimental pressure-side main flow velocity, u_{bulk} , at the plane of the slot exit (Ling et al., 2013). This value is tabulated in Table 1. The contours are shown on a plane 2 mm above the bottom surface as was done by Ling et al. (2013) for data demonstration. The non-dimensionalization method is given by Eq. (1) where u_s is the local coolant velocity:

$$u'_s = \frac{u_s}{u_{bulk}} \quad (1)$$

Because the coolant is injected from the side of the domain at an upstream location, there is an observable asymmetry in the flow field entering the domain. Figure 2 presents the comparison in a portion of the domain demonstrated in Figure 1-b where the plenum section contracts into the constant-height region containing the pin array. According to the orientation of Figure 2, the flow enters the domain from the bottom and from a further upstream location out of the boundaries of the figure, and moves towards right where the slots are located. The effect of this injection is reflected as an increase in the local velocity, both in the contours of the predictions and the data.

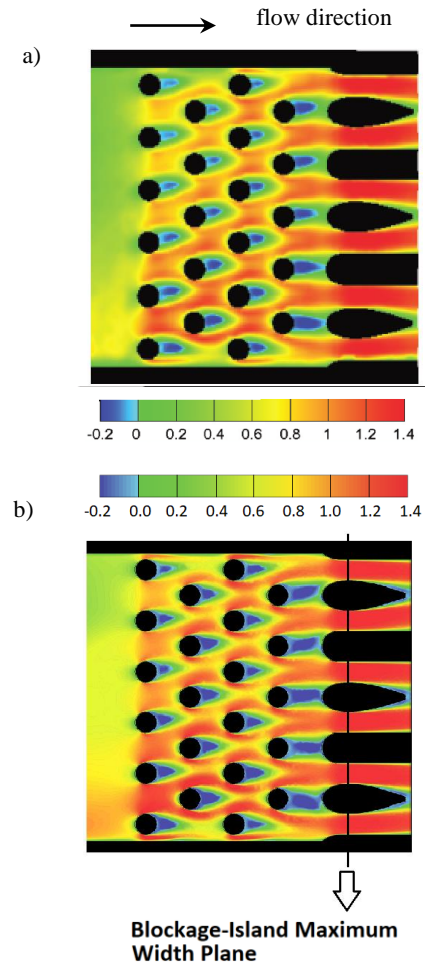


Figure 2. Non-dimensional streamwise velocity contours a) experiment (Ling et al. (2013)), b) predictions

The velocity measurement at the location corresponding to the blockage-island maximum-width is 0.51 m/s (Ling et al., 2014). This value was predicted as 0.52 m/s that gives an over-prediction of approximately 2%. In fact, the velocity predictions are found to be in good agreement with the data over the whole domain of Figure 2. The separation bubbles are observed to form immediately behind every pin fin within the blue regions in a similar fashion to what the data suggests. These wakes extend towards downstream pins, and the velocity is recovered across the remaining sections of each passage. In the wake of the islands, the flow separation is not as obvious. The data contours show that the flow is redistributed through the pin array; and this is observed

in the prediction contours of Figure 2 as well. The only significant difference occurs on the left side of the contours that are closer to the manifold entrance where the coolant is introduced into the test section. The assumed velocity profile and turbulence intensity are likely to cause a difference in the predictions at the immediate vicinity of this part of the domain. However, as was mentioned before, the computational studies performed by Ling et al. (2014) showed that the coolant inlet conditions did not have a significant impact on the predictions.

In the external domain of Figure 1-c, the boundary conditions listed in Table 2 from the experiments of Ling et al. (2013) are matched. The typical velocity-inlet and static pressure-outlet type of boundary conditions were applied on the model. The slot region is modeled as an opening and the velocity profile information is imported from the results of the internal cooling validation part.

Table 2. Experimental conditions from Ling et al. (2014) used for external domain

Main Flow Inlet Velocity	0.19 m/s
Inlet Turbulence Intensity	1%
Inlet Turbulence Length Scale	1 mm
Main Flow Temperature	20 °C
Main Flow Mass Flow Rate	123 l/min

Figure 3 demonstrates the cutback region of the flow domain with half of the slot exit and half of the breakout surface between the neighboring lands. The main flow enters the domain through the inlet in Figure 1-c and the coolant enters the domain through the slot exit.

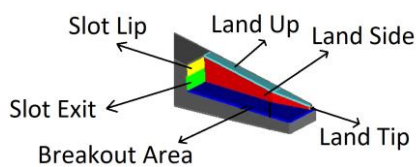


Figure 3. Close-up view of computational domain for slot exit region

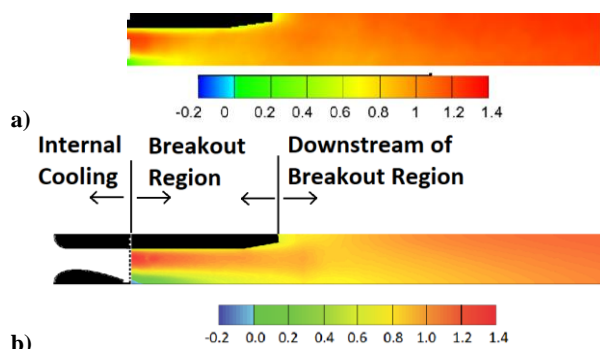


Figure 4. Non-dimensional streamwise velocity contours downstream of slot exit a) experiment (Ling et al. (2013)), b) predictions

The sensitivity study was performed for the meshes with 1.3 M, 3.8 M and 8.4 M elements. The streamwise

velocity profiles on the midsection of the plane 2.5 mm above the breakout region were monitored. The mesh with 3.8 M elements was selected since the average percentage of the difference between the medium and the fine mesh was 2.1% while the difference between the coarse and the medium mesh was 1.5%. First layer thicknesses around the walls are adjusted so that y^+ is kept around 1. 20 layers for tunnel walls and 18 layers for other walls were implemented.

The comparison between the predictions for the flow field downstream of the slot exit and the experimental result of Ling et al. (2013) is shown in Figure 4 in the form of contours of the nondimensional streamwise velocity component. In Figure 4, the coolant enters the domain from the left side where the slot exit is located and then mixes with the main flow. The shown section is the plane 2 mm above the breakout surface and provides a top view of the downstream flow field. The black region represents the solid land. The top and bottom sides are the symmetry walls. The use of the symmetry walls has enabled to cut down the computation time significantly. From Figure 4 it can be seen that the low-momentum wake behind the airfoil-shaped blockages and pin fins extend far downstream in the contours in the predictions. This under-prediction behavior with the $k-\omega$ SST turbulence model is reasoned with the insufficient turbulent viscosity (Ling et al. 2014). Although the mixing process of the coolant with the mainstream flow seems to occur slower in the predictions compared to the experiment, the velocity predictions are generally found to be in good agreement with the data over the whole domain.

Preparation of Comparison Cases

In the internal validation case, the experimental configuration had the coolant injection through the side. For the comparative study, the coolant flow is introduced into the passage directly in the streamwise direction. This made it possible to reduce the size of the computational domain as the flow through the trailing edge internal geometry becomes symmetrical in addition to the symmetry of the geometry itself. Using a plane of symmetry through the centerline of the model, the mesh size was halved. The dimensions of the models used in the study are summarized in Table 3. Four rows of pin fins are placed along the section, with straight lands and airfoil-shaped blockages at the end of the section. An airfoil shape is used for the benefit of separation reduction in the wake.

Table 3. Model dimensions (in mm)

Streamwise Length	79.82
Height	5.00
Diameter of Circular Pins	5.00
Major Axis Length of Elliptical Pins	14.07
Chord of Airfoil-Shaped Pins	14.07
Minor Axis Length of Small Elliptical Pins	1.78
Maximum Thickness Length of Airfoil-Shaped Pins	1.78

The figures presented in this paper will use the initial letters for each pin shape for clarity. In constructing the models shown in Figure 5, the centerlines of pin rows of one configuration were selected to match the centerlines of corresponding rows of the other two configurations. For the models of (b) and (c), the minor axes of the elliptical pins and the maximum thicknesses of the airfoil-shaped pins are adjusted so that they have the length of a circular pin diameter. This way, frontal areas of all shapes were kept the same rather than their circumferences, as was done by Uzol and Camci (2005), guaranteeing the same amount of flow blockage area. For the models of (d) and (e), the major axes of the ellipse and the airfoil-shaped pins matched the diameters of the circular pins. This allowed for pin rows of equal extents for (a), (d), and (e); therefore, the distance between each row of pins as well as the distance between the last row of pins and the slot lands were increased.

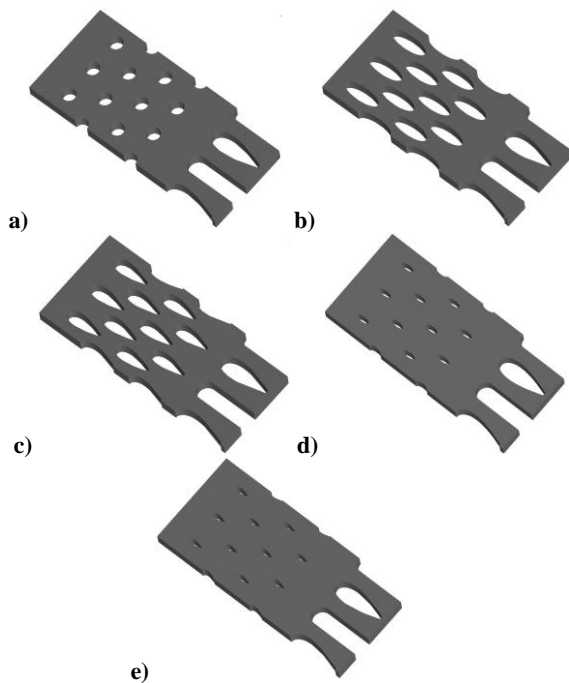


Figure 5. Computational models for the internal section: a) C, b) E, c) A, d) S-E, and e) S-A pins

By introducing these models, it is aimed to observe the effects of both the shape and the relative spacing of the pins. One particular detail about the airfoil-shaped pins is that they are of the same shape of the island blockages at the slot exit, the NACA 0033 profile, but at a smaller scale. Due to its known profile, the maximum thickness determines the chord of this shape. For comparison purposes, the major axis of the elliptical pin shape was taken to be of the chord length.

Figure 6 shows the zoomed-in views at the near-pin locations. The sensitivity studies were performed for the meshes with 650K, 1.6M, and 3.4M elements. The convergence of residual levels was established below 10^{-4} . As is done in the sensitivity study, the velocity, total pressure, and additionally the total temperature values were monitored along the centerline of the pin array. The

average percentage of the difference between the coarse and the medium mesh was 9.7%, and the difference between the medium and the finer mesh was 9.1% for the circular-pin case. Again, these percentages are magnified due to low velocities. On the other hand, the comparison of total pressure and total temperature values between the meshes gave considerably small differences of 0.14% and 0.5% on average, respectively. Hence, the mesh with 1.6M elements was selected for the rest of the comparison study. In order to highly resolve the boundary layer, $y^+ < 1$ condition was established for all pin shapes. 30 layers of prism elements were constructed with a first-layer height of 0.0008 mm.

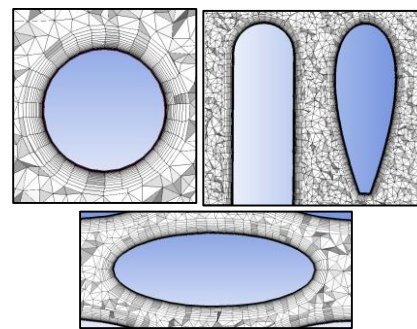


Figure 6. Meshes used in internal comparative study

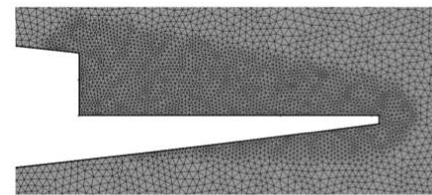


Figure 7. Mesh used in external comparative study

Figure 7 shows the mesh used in the external comparative study. There was no change in the model shown in Figure 1-c between the cases. The first-cell height of all walls is taken as 0.0011 mm. For the mesh sensitivity study, the meshes with 2.7M, 6M and 14.2M elements are used. The mesh with 6M elements is selected since the difference between the coarse and the medium mesh was 5.2% while it was 1.7% between the medium and the fine mesh.

RESULTS AND DISCUSSION

Internal Cooling

The computations are performed for the selected boundary conditions that reflect the actual engine operation. For this purpose, the experimental measurements that were obtained by Hylton et al. (1983) for the C3X cascade vane were utilized. In that program, the independent parameters such as Mach number, Reynolds number, wall-to-gas temperature ratio, and turbulence intensity were varied in ranges consistent with the engine environment. Using this data set, the necessary boundary conditions to perform the computations were either adopted directly from Hylton et al. (1983) or were calculated if they were not readily available.

Table 4. Boundary conditions

Air Inlet Velocity	31.1 m/s
Air Inlet Temperature	478.2 K
Wall Temperature	614.2 K
Outlet Static Pressure	332.1 kPa

A summary of these conditions is given in Table 4. The inlet turbulence intensity was kept at 5% as in the validation case. Air inlet velocity was taken to be uniform. All solid walls were modeled using the no-slip boundary conditions with a constant temperature of approximately 614 K. The fluid domain is modeled as a calorically perfect ideal gas with a specific heat capacity of 1004.4 J/kg.K at constant pressure and a dynamic viscosity of 1.831×10^{-5} kg/m.s. All results presented in this section represent the predictions over one half of the computational domain only, which is cut through the centerline. In the contour plots, the presented plane is the mid-plane (2.5 mm) across the section height.

Aerodynamic results

Figure 8 shows the streamwise velocity contours at the mid-plane. Similar to the validation case in Figure 2, as the flow proceeds through the passage, the regions of reverse flow are formed behind every pin fin. Since the inlet flow is introduced in the streamwise direction and is assumed to be uniform, the flow distribution reflects this inlet condition in the downstream region. The top side of each contour plot is a physical wall while the bottom side is a symmetry wall. Therefore, the local flow features along these two sides are not necessarily symmetric due to the endwall effects occurring along the top side only. On the other hand, the flow field is symmetric with respect to the symmetry wall, but the other half of the domain is not shown in the figure.

Although the velocity gradients through the circular pin array are mild, they become more significant for the pin shapes of (b) ellipse and (c) airfoil profile. The separation regions are intensified at the last row of pins for these cases. This is mostly due to the relatively short distance between the pin and the blockage surfaces, as well as the lack of another follow-up pin row. While the circular pin rows are totally isolated from each other across the array, (b) elliptical, and (c) airfoil-shaped pin rows are not. Hence, the reduced flow area in between the trailing edge of one row and the leading edge of its downstream row causes an increase in the local velocity. On the other hand, the wakes of the airfoil-shaped pins across the pin array of case (c) are not obvious, since an airfoil shape will have a reduced separation zone compared to a blunt object such as cylinder or ellipse. For cases (d) and (e), since the pins are of a smaller size having the same row extents with those of case (a), the interaction between each row is not as significant anymore.

The velocity increases in the flow direction in general, reaching its maximum through the blockage area. Large velocity gradients are observable in this region towards the slot exit both in streamwise and spanwise (along the section width) directions. Due to the overlaps between

the rows of cases (b) and (c), the interaction between the pins contribute to the velocity gradients as well. In other words, if the rows are separated from each other, the velocity gradients diminish as is shown in cases (d) and (e). For those cases, a significant velocity gradient is observable only through the blockage area.

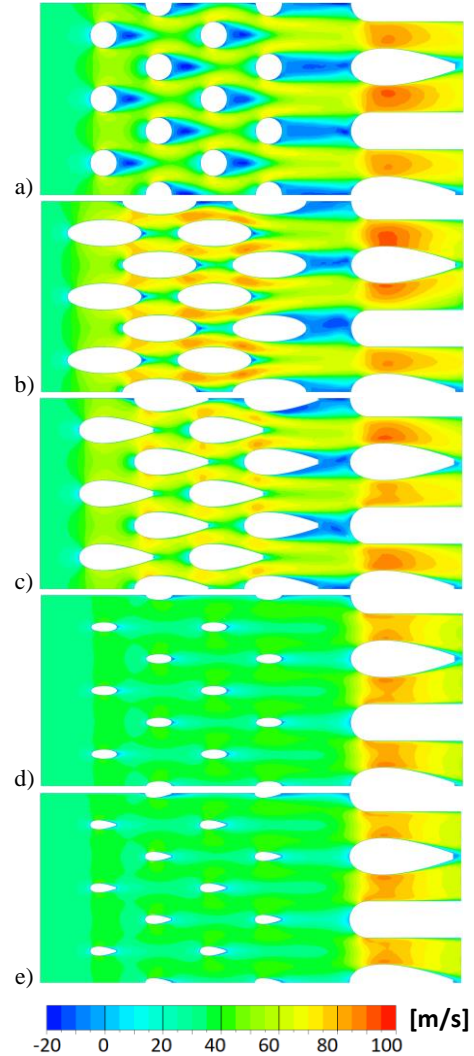


Figure 8. Streamwise velocity contours: a) C, b) E, c) A, d) S-E, and e) S-A pins

In order to have more information on the flow patterns, the streamwise vorticity contours in the mid-plane are examined in Figure 9. Vorticity is non-dimensionalized by the air inlet velocity and the section height. The non-dimensionalization method is given by Eq. (2), where H is the channel height, u_i is the inlet velocity, and the subscript s defines the streamwise direction:

$$\omega'_s = \frac{\omega_s H}{u_i} \quad (2)$$

The neighborhood of each pin across an array is dominated by the vortical flow structures. The blunt shape of the circular pin is the one producing the largest wake region where the flow separation occurs. In addition, there are horseshoe vortices occurring along the

surfaces of the pins, coinciding with the strong vorticity regions. The wake of the airfoil-shaped pin (c) is significantly smaller than those of (a) and (b), meaning a reduced aerodynamic penalty. With the reduced size of the pins (d) and (e), this penalty is even lower.

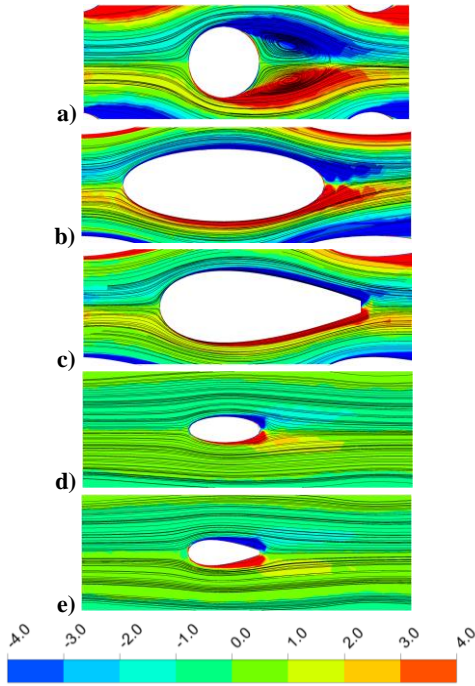


Figure 9. Non-dimensionalized streamwise vorticity contours: a) C, b) E, c) A, d) S-E, and e) S-A pins

Flow features can be examined by looking at the total pressure coefficient, which gives a measure for the total pressure drop in streamwise direction via Eq. (3)

$$\psi = \frac{(P_T - P_{T,l})}{\rho_l u_l^2 / 2} \quad (3)$$

In Figure 10, this coefficient is mass flow-averaged across the width of the domain, and is shown as a function of the normalized distance from the inlet. To do so, a series of vertical cut planes at different downstream locations were used. Then, the mass flow-average values of ψ were calculated on these planes. Since there are large velocity variations in the lateral direction, mass flow-averaging was preferred rather than spanwise-averaging to better quantify the parameters of interest, such as loss and entropy generation. The four vertical dashed lines show the locations of the pin centers, which are the same for all five configurations. Figure 10 shows that starting off with the same inlet total pressure, all three configurations cause a consistent increase in ψ due to the loss accumulation across the domain. The configuration with the elliptical pins seems to have the highest amount of loss, followed by the circular pins and the airfoil-shaped pins. Although this seems contrary to the findings of Uzol and Camci (2005) regarding the performance of elliptical and circular pins, the elliptical pins in this study have significantly larger wetted areas resulting in higher viscous dissipation and hence higher losses. However, even if the airfoil-shaped pin has also a

large wetted area, the lessened aerodynamic penalty for this shape is remarkable. For the small size elliptical and airfoil-shaped pins, the aerodynamic penalty is significantly less due to the shrinkage in the surface area.

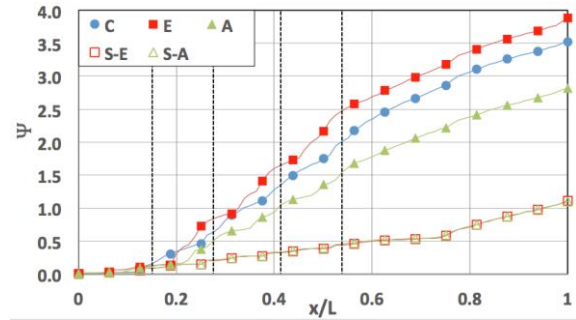


Figure 10. Mass flow-averaged ψ in streamwise direction

More insight into the loss mechanism can be gained if the entropy generation across the domain is analyzed. Figure 11 demonstrates the top view of the section mid-plane with the entropy contours. The general trends show a consistent entropy generation in the streamwise direction for all five configurations. Substantial losses in the domain occur by the walls due to the effects of viscosity, which is indicated by the red color. When the flow reaches the trailing edges of the airfoil-shaped pin and blockage surfaces, losses add up due to the local acceleration and mixing of the surface flows. This is more significant at the blockage trailing edges. The entropy generation is the largest for the elliptical pins, followed by the circular pins due to the large wake regions behind the pins. It is hard to distinguish the contours of the small elliptical and airfoil-shaped pins. Hence, their loss characteristics are very similar.

In order to quantify the loss amount for each configuration in more detail, the computational domain is split into six regions, as in Figure 12-a. Region A represents the inlet section, Region B is the pin array, and Region C consists of the remaining portion with the lands and the blockages. The layout given here shows the five configurations superimposed on top of each other. The split planes are located approximately a one-pin diameter (1D) away from the row centerlines. The first and last planes are further away from the nearby centerlines, approximately 1.5D and 2D, respectively, in order to include the extensions of the larger pin shapes. Region B is further split into row-by-row sections. Due to the dimensions of the shapes, the circular pins remain between the planes, while the leading edge of the large elliptical pins and the trailing edge of the large airfoil-shaped pins run over the planes. However, with this approach the loss quantification can be simplified reasonably.

For the loss audit, the mass flow-averaged entropy value for each cutting plane (s_l , l for local) was compared with the mass flow-averaged entropy value of the previous plane (s_{up} , up for upstream), according to Eq. (4):

$$Total\ Loss\ \% = \frac{S_l - S_{sup}}{S_e - S_i} \times 100 \quad (4)$$

where the difference is normalized by the total increase between the inlet and exit planes of the domain.

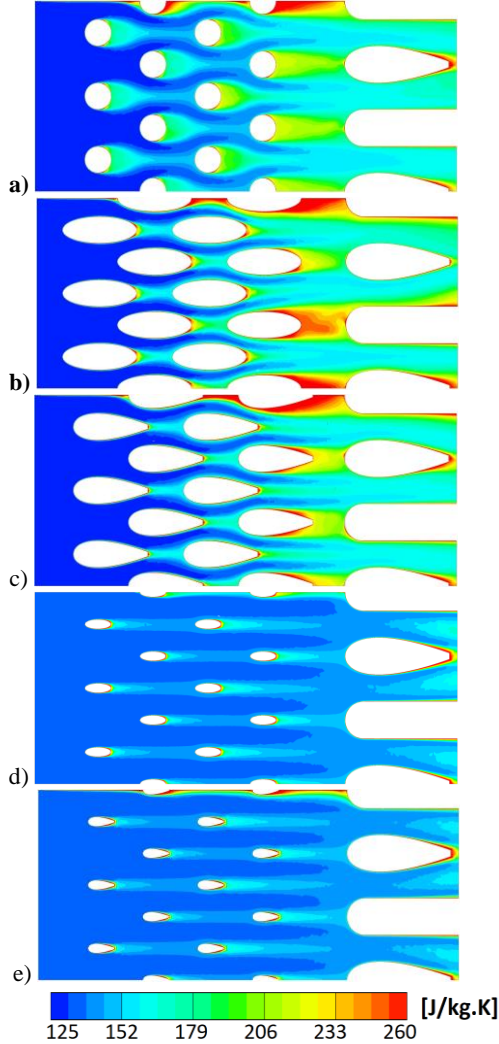


Figure 11. Entropy contours: a) C, b) E, c) A, d) S-E, and e) S-A pins

The loss amount does not accumulate much in Region A, as this is the shortest region and there are no cross-pin effects due to the absence of the pin structures. As the flow starts going through the pin array, a significant rise occurs in the loss for all configurations, and the loss stays at similar levels across the pin rows. All pins experience elevated levels of entropy generation in Region B4. This region is where the wakes of pins are strongly experienced due to a combined effect of the absence of another downstream row of pins and the interaction with downstream lands and blockages that are located in close proximity. Finally, the largest amount of losses for all five configurations occurs in Region C.

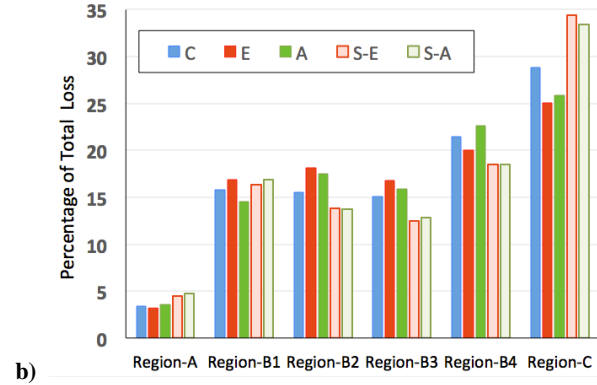
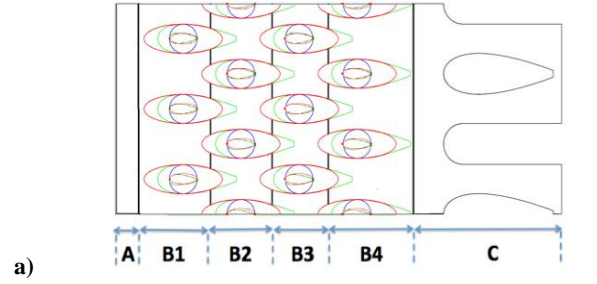


Figure 12. Loss audit across trailing edge: a) domain regions, b) loss split per region

Figure 12-b provides information on the loss split across the domain for each configuration, but it does not compare the loss amounts between configurations. For this, the maximum mass flow-averaged entropy on the exit split plane across all five configurations is used to normalize the local mass flow-averaged entropy on the planes splitting the domain. This is defined as the entropy ratio on the y-axis of Figure 13, and its variation is given as a function of x/L . The vertical dashed lines are attached to the plot to identify the pin locations.

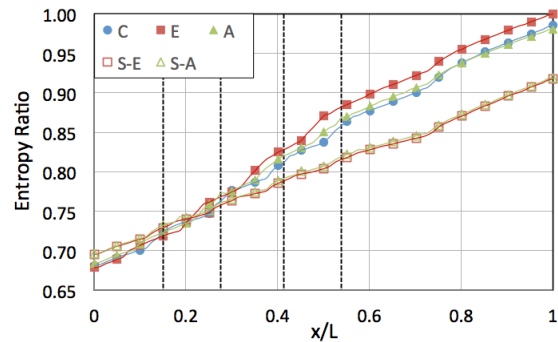


Figure 13. Mass flow-averaged entropy in streamwise direction

Figure 13 presents the mass flow-averaged entropy values, with similar trends to ψ variation of Figure 10. Comparing the general trends in these figures, it is clear that the overall loss generation is greater for the elliptical pins, leading the circular and airfoil-shaped pins by a small difference of around 2%. The small pins generate less penalty. It can be concluded from this discussion that losses could be reduced if the downstream slot section was kept further apart from the last row of pins for the given pin dimensions relative to the domain. Since the rows were not totally isolated for the elliptical and airfoil-shaped pins, the interaction between the rows also

contributes to the overall loss mechanism. The losses are further reduced if the pins are of smaller size. The difference between the two small pins is almost negligible, and their curves are almost identical. They provide aerodynamics savings of approximately 7-8% compared to their larger size partners.

Thermal results

The convection heat transfer coefficient, h , was evaluated on the upper wall of the domain. For the calculations, Eq. (5) is used:

$$q'' = h x (T_{wall} - T_{bulk}) \quad (5)$$

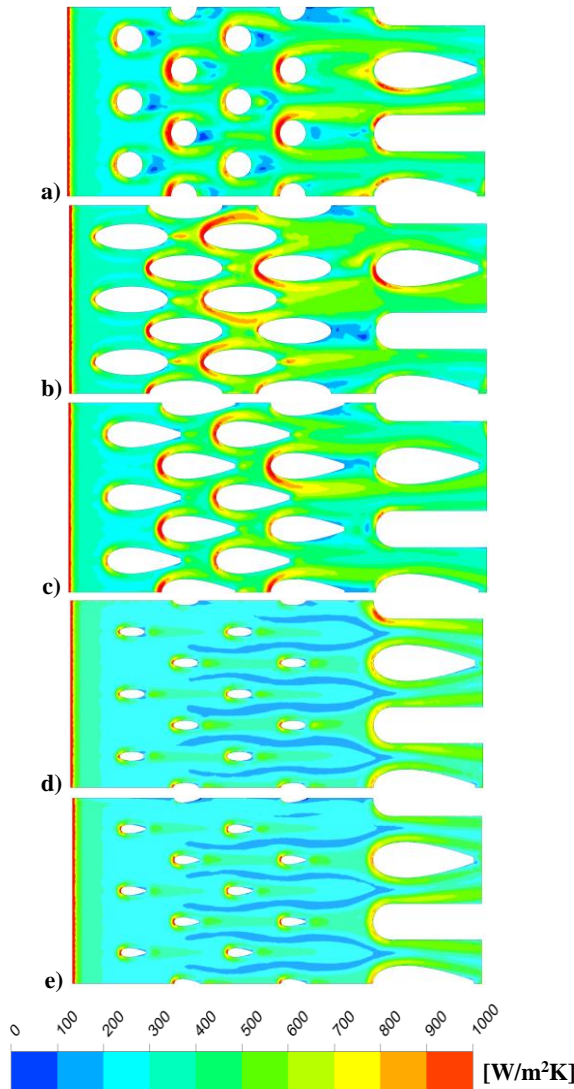


Figure 14. Heat transfer coefficient contours: a) C, b) E, c) A, d) S-E, and e) S-A pins

The bulk temperature was calculated as the mass flow-averaged temperature on the spanwise planes in order to take into account the streamwise temperature of the coolant. Additionally, Nusselt number was calculated using Eq. (6):

$$Nu = \frac{h x D}{k_f} \quad (6)$$

where D is the pin diameter, and k_f is the thermal conductivity of air as the working fluid.

According to Figure 14, the heat transfer coefficient contours give the highest levels at the stagnation locations on the pin surfaces as well as on the downstream blockage frontal areas. The horseshoe vortices rolling up around the pin surfaces coincide with the traces of high heat-transfer regions. The levels are reduced significantly for the smaller size pins, hinting that the heat transfer performance of these pins will not be as good.

Validation of heat transfer

Another validation for the internal solution is performed for the heat transfer predictions. The results are presented in terms of Nusselt number, and are compared to the data set provided by Metzger et al. (1986). This data is presented in Figure 15-a.

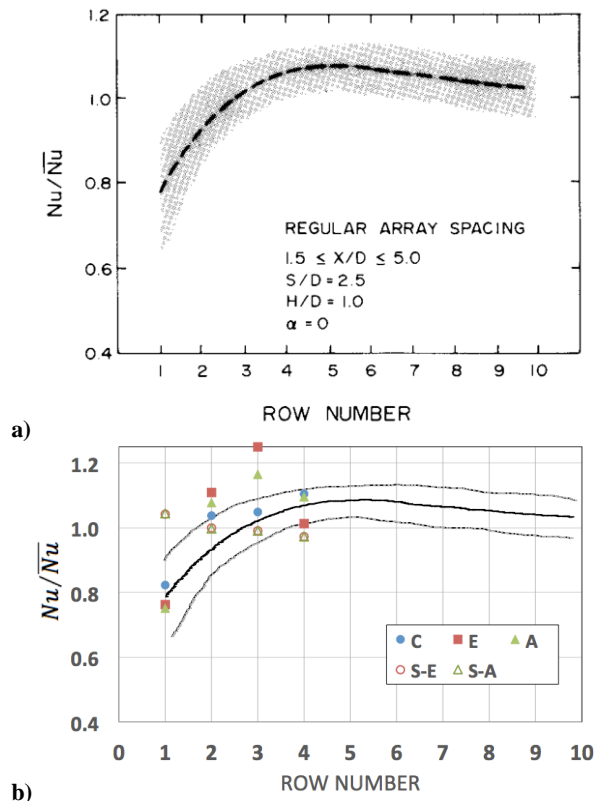


Figure 15. Normalized Nusselt numbers for pin arrays: a) experiment (Metzger et al. (1986)), b) predictions

In this study, Metzger et al. (1986) defines a row-averaged Nusselt number (Nu) and an array-averaged Nusselt number (\overline{Nu}). The shaded band consists of the data from circular pins with Reynolds number ranging from 2310 to 51740. Figure 15-b shows the prediction results with respect to this band. The pin-array structures had $X_p/D=2.4$, $S_p/D=2.4$, and $H_p/D=1$. The flow Reynolds number was calculated to be 52375.

Considering that these values are within close range of the data of Figure 15-a, a comparison can be performed with the predictions of this study. The prediction results reasonably fell into or around the shaded band, especially showing a good agreement for the circular pins. Only one data point from the circular pin set falls slightly out of the band by 1%. The maximum outlier for the airfoil-shaped pins is around 7%, which is followed by the elliptical and the two small pins with a value of around 15% each. Considering that the data in this band represent the circular pins, the observable mismatch of the predictions for the other pins is understandable.

External Cooling

For the comparison cases, the boundary conditions are taken from the measurements of Hylton et al. (1983) for the C3X cascade vane. The approach that was previously described for the external section is used here. The velocity profiles and the static temperatures at the slot exit from the internal section analysis of the pin shapes are used as the boundary conditions. The static temperatures are given in Table 5 and the velocity profiles are presented in Figure 16.

Table 5. Mass flow-averaged slot static temperatures for different pin shapes (in K)

Circular	504.2
Elliptical	505.5
Airfoil-Shaped	505.1
Small Elliptical	498.6
Small Airfoil-Shaped	498.8

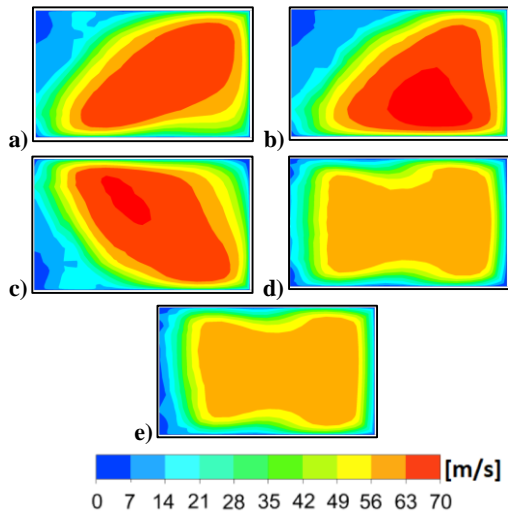


Figure 16. Slot exit velocity profiles: a) C, b) E, c) A, d) S-E, and e) S-A pins

The inlet velocity is calculated as 95.32 m/s from the inlet Mach number given in the data set (Hylton et al., 1983) and this same value is used for all five cases. The inlet turbulence level is set as 8.3% and the inlet total temperature is taken as 782 K. The outlet pressure is iterated to match the average static pressure at the slot exit with the boundary condition supplied at the internal comparison case, giving a value of 307.8 kPa. All solid

walls are modeled using the no-slip boundary conditions and they are treated as adiabatic. The approach for thermal boundary conditions is taken from Martini et al. (2006).

Aerodynamic results

Figure 17 shows the streamwise velocity contours at the mid-plane above the half of the breakout surface between the lands for all five configurations. Reverse flow regions due to mixing are observed at the land tip and locally in the breakout region. Further downstream of the slots, the velocity increases in the flow direction. Flow patterns for all cases are the same further downstream of the breakout region, but they show minor differences near the slot exit.

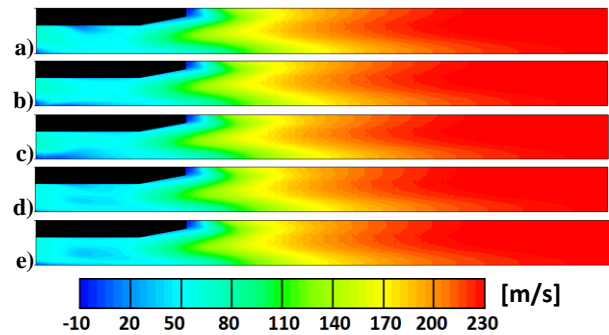


Figure 17. Streamwise velocity contours downstream of slot exit: a) C, b) E, c) A, d) S-E, and e) S-A pins

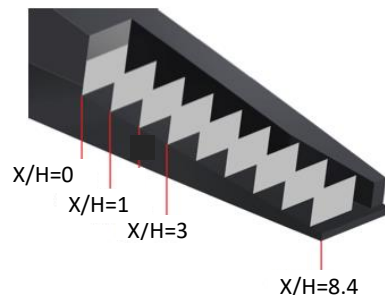


Figure 18. Breakout surface scan with vertical planes

Next, the development of the flow on the breakout surface is analyzed. The region is scanned via planes perpendicular to the streamwise direction at every 5 mm (H) distance starting from the slot exit as shown in Figure 18, where H is the slot exit height. The left side of the figure is a symmetry wall, while the right side is a solid land wall. Figure 19 shows the non-dimensional streamwise vorticity contours at the slot exit. Vorticity is non-dimensionalized by the section height and air inlet velocity via Eq. (2). The regions represented by the negative values in the color legend indicate a clockwise rotation while the regions with positive values indicate a counterclockwise rotation. Circular and elliptical pins show similar vortical structures while the airfoil-shaped pins generate reversed vortices near the symmetry wall. The large vortical structures observed become smaller for the small size pins due to the longer distance between the slot exit and the last row of small pins.

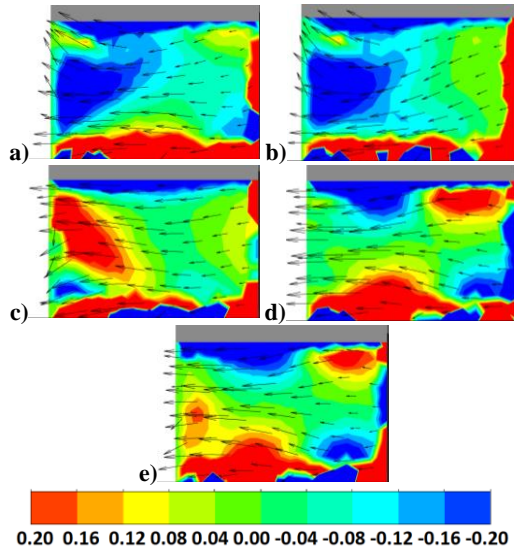


Figure 19. Streamwise non-dimensional vorticity contours at slot exit: a) C, b) E, c) A, d) S-E, and e) S-A pins

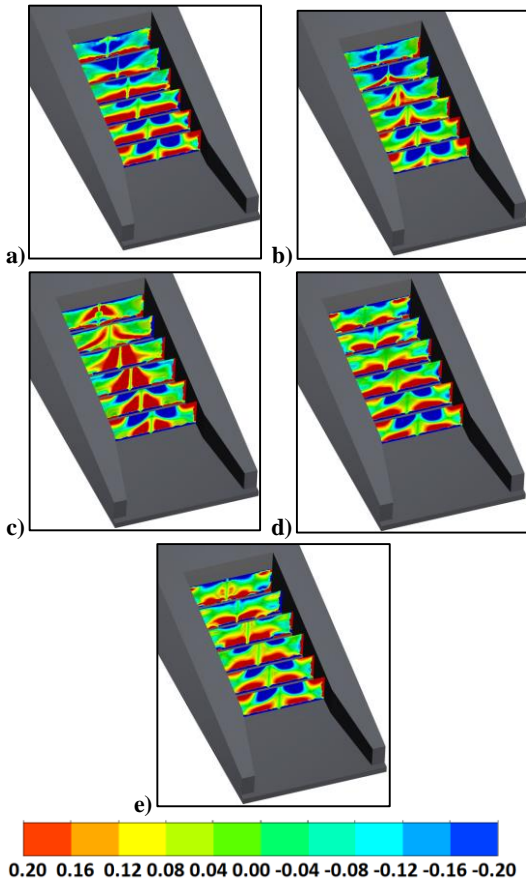


Figure 20. Streamwise non-dimensional vorticity contours downstream of slot exit: a) C, b) E, c) A, d) S-E, and e) S-A pins

The development of the flow field on the breakout surface is summarized in Figure 20 using the vertical planes. Moving downstream of the slot exit, the variation in the flow patterns indicates the interaction between the main flow and the coolant blown out from the slot exit. The flow patterns continue to establish downstream of each pin up to around $X/H=3$ where the effect of pin shapes is observable. This establishment is also visible in the velocity contours of Figure 17. Beyond this location,

the effect of pin shapes seems to be diminishing, especially for the circular and small pins, but some differences are still observable for the elliptic and airfoil-shaped pins due to the interaction existing between those pin rows. Also, there are only minor differences here in the size of the vortical structures for each case. In the last plane of Figure 20, the flow features for all cases are looking similar as the main flow conditions suppress the impact of the coolant flow and dominate the flow region.

Thermal results

The total temperature contours downstream of the slot exit are given in Figure 21 for the elliptical and small-elliptical pin shapes only, since all cases show very similar trends. At the slot exit, the coolant temperature levels are low and they increase in the flow direction due to the mixing of the coolant with the surrounding hot mainstream. Total temperature levels are observed to be lower for the small pins since the inlet coolant temperatures are lower. On the last plane, the maximum temperature reaches well beyond 720 K.

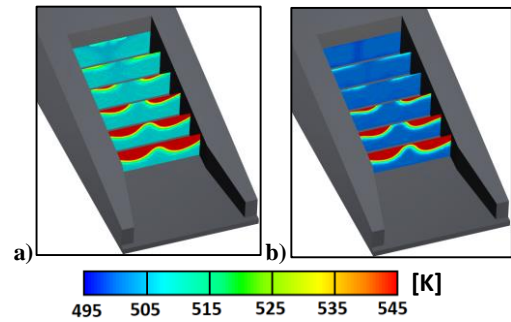


Figure 21. Total temperature contours downstream of slot exit: a) E and b) S-E pins

The performance of film cooling can be demonstrated with the use of film-cooling effectiveness. It is calculated with Eq. (7) where T_∞ is the mainstream temperature of 777.5 K, T_{wall} is the wall temperature calculated by the CFD analysis with adiabatic boundary condition, and T_c is the coolant temperature calculated as the mass flow-averaged static temperature at the slot exit that was obtained from the calculations for internal cooling:

$$\eta = \frac{T_\infty - T_{wall}}{T_\infty - T_c} \quad (7)$$

Film-cooling effectiveness levels are generally high all across the breakout surface for all pins. Figure 22 shows the slight local variations with contours. Right at the slot exit the effectiveness levels are the highest and they decrease in the flow direction. Given that the coolant static temperatures listed in Table 5 vary only within 7K, the variation in the effectiveness levels is small as well. For the small elliptical and small airfoil-shaped pins, the effectiveness shows a relatively slower decrease. Due to the relatively lower heat-transfer performance of these pins in the internal channel, the coolant temperature did not increase until the slot exit as much resulting in higher film effectiveness for external cooling. Since the coolant

temperature for the elliptical pins turned out to be the highest at the slot exit among all cases, the local film-cooling effectiveness levels for these pins are the lowest.

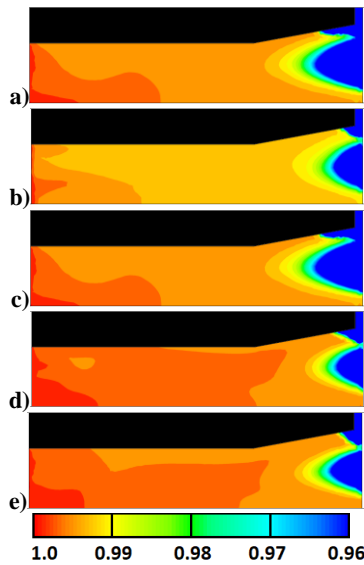


Figure 22. Film-cooling effectiveness contours on breakout surface: a) C, b) E, c) A, d) S-E, and e) S-A pins

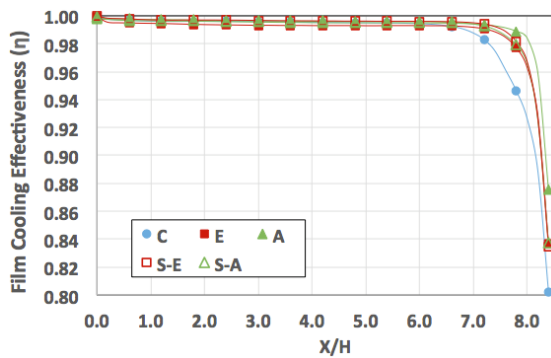


Figure 23. Laterally-averaged film-cooling effectiveness on breakout surface

To compare the overall film-cooling performances of different pin shapes, the film-cooling effectiveness along the breakout surface is averaged in the lateral direction and shown in Figure 23. The horizontal axis shows the ratio of the axial distance from the slot exit (X) to the slot height (H). $X/H=0$ is the slot exit, and $X/H=8.4$ is the end of the breakout surface. Considering the slight local variations shown in Figure 22, no significant difference can be observed between these cases when the values are further averaged. At the domain exit, a larger difference seems to exist for the circular pins followed by the airfoil-shaped pins, but this variation is rather due to the existence of large effectiveness gradients in this section of the flow region ($X/H>6.5$).

Figure 24 shows the film-cooling effectiveness contours on the side wall of the land. The coolant is ejected over the breakout surface right at the slot exit, while the mainstream flow partially fills this section that is split with the slot lip located above the slot exit. The effect of this mainstream flow is shown with the blue region. The thermal patterns of the coolant flow and the mainstream

mixing are similar for all cases. As for the breakout surface film-cooling effectiveness levels, the land side film-cooling effectiveness levels are directly related to the slot exit temperatures of the coolant.

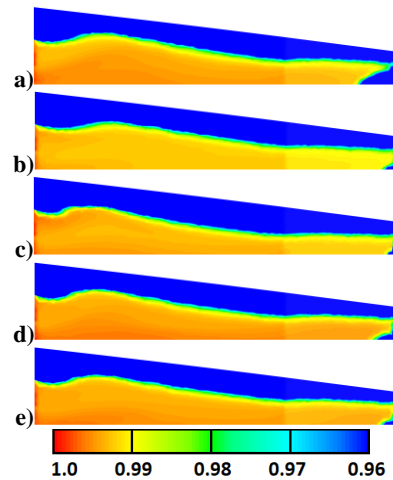


Figure 24. Film-cooling effectiveness contours on land side: wall, a) C, b) E, c) A, d) S-E, and e) S-A pins

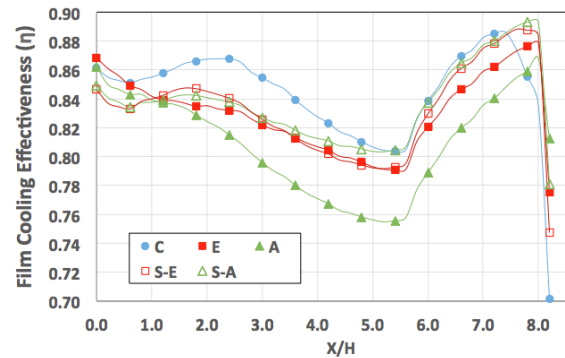


Figure 25. Laterally-averaged film-cooling effectiveness on land side wall

Figure 25 shows the laterally-averaged film-cooling effectiveness on the side wall of the land. Here, averaging is done over the height of the side wall. As was observed on the breakout surface, on the side of the land, the elliptical, small elliptical, and small airfoil-shaped pins perform similarly across the region, while the thermal performance is relatively higher for the circular pins and relatively lower for the airfoil-shaped pins. Up to $x/H=5.5$, the film-cooling effectiveness for all cases show an expected decreasing trend, but beyond this point the levels start increasing. This location is where the breakout surface opens up in the lateral direction. It is likely that this change in the geometry causes the lower-momentum fluid to provide a better coverage on the side walls.

Selection of Optimum Pin-Fin Configuration

Figure 26 and Figure 27 summarize the trade-off that will need to be considered between the pressure loss and thermal features of the pin-fin arrays in the internal and external sections, respectively. In Figure 26, the bars represent the ratios of the array averages to the overall average of all five pin arrays, for Nusselt number and for total pressure loss. An array average consists of the

regions B1, B2, B3, and B4. According to this comparison, the airfoil-shaped pins bring aerodynamics savings due to their significantly reduced wake region, compared to the pins of similar size. For the two small-size pins, the differences between the aerodynamics and thermal characteristics are not distinguishable. Although the pressure loss is significantly reduced, the heat transfer performance is reduced as well. Hence, this result shows that there is no one correct answer to the selection of the optimal cooling configuration. The decision should be made according to the needs of the design.

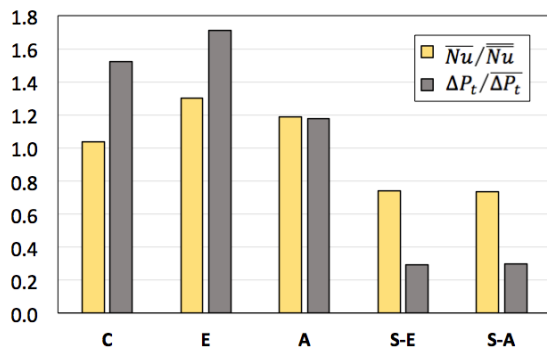


Figure 26. Loss and thermal comparison of pin arrays in internal section

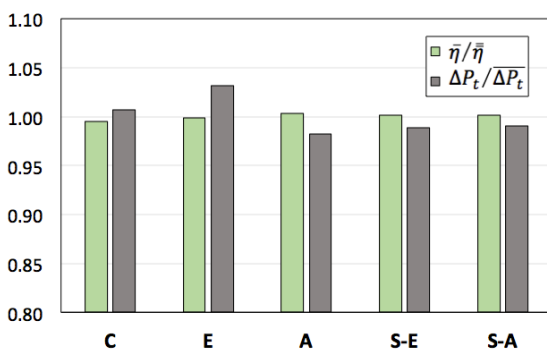


Figure 27. Loss and thermal comparison of pin arrays in external section

In Figure 27, the bars filled with diagonal stripes represent the ratio of total pressure loss between the slot exit and the end of the blade (end of the breakout surface) to the average total pressure loss of all five pin arrays. The black bars represent the ratio of the film-cooling effectiveness average for each array to the overall average of all five pin arrays in the breakout region. Considering the slight variations shown in Figure 27, all pin configurations are observed to give almost the same thermal performance, while the pressure loss levels are slightly above the average value for the elliptical and circular pins. This comparison shows that the overall aerodynamic and thermal performances of film cooling on the breakout surface of the trailing edge region are weakly dependent on the flow structure introduced in the slot exit region following the internal pin array.

CONCLUSIONS

This study has focused on pin fin and slot film cooling used in blade trailing edge design. The computations

were performed to determine the most advantageous combination of shape and size of pin arrays from an aerodynamics and a thermal perspective. Five different configurations were considered for the analysis of flow features, losses and heat transfer inside of the pin array and on the external surface downstream of the slot exit.

The local features in the flow field of the internal cooling section showed that the largest total pressure drops occur in and around the pin wakes in the streamwise direction. The last row of pins, where the elliptical and airfoil-shaped pins stayed relatively closer to the leading edge of the downstream lands and islands, the flow field experienced stronger and wider zones of flow separation resulting in substantial loss generation for this size of pins. The local features showed that the losses keep adding up through the pin array. Despite its larger wetted area, the airfoil-shaped pin was found to have less aerodynamic penalty mostly due to the separation reduction in its wake region, while its thermal performance was at similar levels to those of similar size. On the other hand, the smaller-size pins produced less amount of loss as expected; however, this is accompanied with a reduction in thermal performance in return.

Minor differences were located in the velocity contours in the breakout region. The streamwise vorticity contours spanning the downstream region of the trailing edge slot exit revealed that the influence of different coolant inlet conditions starts to diminish approximately around 15 mm (3H) downstream of the slot exit, and beyond that point the general trends of the flow structure for all pin shapes look similar. The comparison of pressure coefficients showed that all pin shapes have also very similar pressure loss trends. The small-sized pins were found to reach the highest local film-cooling effectiveness values right on the breakout surface due to the lower temperature at the slot exit, but the laterally-averaged values of all pin shapes were very similar.

With the goal of choosing an optimum pin-fin configuration that is advantageous for slot film cooling from both aero and thermal aspects, this study provides a thorough investigation of the trailing-edge section inside and out that would be of interest to the turbine designers. Among the studied configurations was the airfoil-shaped pins of NACA 0033 that have not been studied before within an array of pins for similar purposes to the authors' knowledge. According to the varying aerodynamic and thermal performances of the pins across the internal and external sections, it is inferred that there is no one correct answer to the selection of the optimal cooling configuration, and the decision should be made according to the needs of the design. Performing an optimization on the size of the airfoil-shaped pins could be a promising approach. With recent advances in the additive manufacturing, the implementation of any random shape into the flow path design seems feasible nowadays. For this reason, future studies focusing on either trailing-edge design, or on any component design in general, seem to have room to investigate the use of novel shapes in turbomachinery design.

REFERENCES

- Ames, F. E., and Dvorak L. A., 2006, Turbulent Transport in Pin Fin Arrays: Experimental Data and Predictions, *J. of Turbomachinery*, Vol.128, No.1, pp.71-81.
- ANSYS CFX-Solver Theory Guide, Release 18.2, Canonsburg, PA, ANSYS, Inc., 2017.
- Armstrong, J., and Winstanley, D., 1988, A Review of Staggered Array Pin Fin Heat Transfer for Turbine Cooling Applications, *J. of Turbomachinery*, Vol.110, No.1, pp.94-103.
- Arora, S., and Abdel-Messeh, W., 1990, Characteristics of Partial Length Circular Pin Fins as Heat Transfer Augmentors for Airfoil Internal Cooling Passages, *J. of Turbomachinery*, Vol.112(3), pp.559-565.
- Benson, M., Elkins, C., Yapa, S., Ling, J., Eaton, J., 2012, Effects of Varying Reynolds Number, Blowing Ratio, and Internal Geometry on Trailing Edge Cutback Film Cooling, *Exp. Fluids*, Vol.52(6), pp.1415-1430.
- Brigham, B. A., and VanFossen, G. J., 1984, Length-to-Diameter Ratio and Row Number Effects in Short Pin Fin Heat Transfer, *J. of Engineering for Gas Turbines and Power*, Vol.106, pp.241-245.
- Chen, Z., Li, Q., Meier, D., Warnecke, H.-J., 1997, Convective Heat Transfer and Pressure Loss in Rectangular Ducts With Drop-Shaped Pin Fins, *J. of Heat and Mass Transfer*, Vol.33(3), pp.219-224.
- Chyu, M. K., 1990, Heat Transfer and Pressure Drop for Short Pin-Fin Arrays With Pin End Wall Fillet, *J. of Heat Transfer*, Vol.112, No.4, pp.926-932.
- Chyu, M., Hsing, Y., Natarajan, V., 1998, Convective Heat Transfer of Cubic Fin Arrays in a Narrow Channel, *J. of Turbomachinery*, Vol.120, pp.362-367.
- Fernandes, R., Ricklick, M., Prasad, A., and Pai, Y., 2017, Benchmarking Reynolds Averaged Navier-Stokes Turbulence Models in Internal Pin Fin Channels, *J. of Thermophysics and Heat Transfer*, Vol.31, No.4, pp.976-982.
- Han, J. C., Dutta, S., and Ekkad, S., 2013, *Gas Turbine Heat Transfer and Cooling Technology*, 2nd ed., CRC Press, Boca Raton, FL, pp.1-26.
- Horbach, T., Schulz, A., Bauer, H.-J., 2010, Trailing Edge Film Cooling of Gas Turbine Airfoils Effects of Ejection Lip Geometry on Film Cooling Effectiveness and Heat Transfer, *Heat Transfer Research*, Vol.41, No.8.
- Horbach, T., Schulz, A., Bauer, H.-J., 2011, Trailing Edge Film Cooling of Gas Turbine Airfoils External Cooling Performance of Various Internal Pin Fin Configurations, *J. of Turbomachinery*, Vol.133, No.4, p.041006.
- Hylton, L. D., Mihelc, M. S., Turner, E. R., Nealy, D. A., York, R. E., 1983, Analytical and Experimental Evaluation of the Heat Transfer Distribution Over the Surfaces of Turbine Vanes, NASA, Contractor Report 168015.
- Kacker, S., and Whitelaw, J., 1969, An Experimental Investigation of the Influence of Slot-Lip Thickness on the Impervious-Wall Effectiveness of the Uniform-Density, Two-Dimensional Wall Jet, *Int. J. of Heat and Mass Transfer*, Vol.12, No.9, pp.1196-1201.
- Li, Q., Chen, Z., Flechtner, U., Warnecke, H.-J., 1998, Heat Transfer and Pressure Drop Characteristics in Rectangular Channels With Elliptic Pin Fins, *Int. J. of Heat and Fluid Flow*, Vol.19(3), pp.245-250.
- Ligrani, P. M., and Mahmood, G. I., 2003, Variable Property Nusselt Numbers in a Channel with Pins, *J. of Thermophysics and Heat Transfer*, Vol.17, No.1, pp.103-111.
- Ling, J., Yapa, S. D., Benson, M. J., Elkins, C. J., Eaton, J. K., 2013, Three-Dimensional Velocity and Scalar Field Measurements of an Airfoil Trailing Edge With Slot Film Cooling: The Effect of an Internal Structure in the Slot, *J. of Turbomachinery*, Vol.135(3), pp.031018.
- Ling, J., Elkins, C., and Eaton, J., 2014, *Improvements in Turbulent Scalar Mixing Modeling for Trailing Edge Slot Film Cooling Geometries: A Combined Experimental and Computational Approach*, Stanford University, Report No. TF-138, CA.
- Ling, J., Elkins, C. J., Eaton, J. K., 2015, Optimal Turbulent Schmidt Number For RANS Modeling of Trailing Edge Slot Film Cooling, *J. of Engineering for Gas Turbines and Power*, Vol.137(7), pp.072605.
- Martini, P., Schulz, A., Bauer, H. J., Whitney, C. F., 2006, Detached Eddy Simulation of Film Cooling Performance on the Trailing Edge Cutback of Gas Turbine Airfoils, *J. of Turbomachinery*, Vol.128(2), pp.292-299.
- Menter, F.R., Kuntz, M., Langtry, R., 2003, Ten Years of Industrial Experience With the SST Turbulence Model, In *Proceedings of the 4th International Symposium on Turbulence, Heat and Mass Transfer*, Turkey, pp.625-632.
- Metzger, D., Fan, C., Haley, S., 1984, Effects of Pin Shape and Array Orientation on Heat Transfer and Pressure Loss in Pin Fin Arrays, *J. of Engineering for Gas Turbines and Power*, Vol.106, pp.252-257.
- Metzger, D., Shepard, W., Haley, S., 1986, Row Resolved Heat Transfer Variations in Pin-Fin Arrays Including Effects of Non-Uniform Arrays and Flow Convergence, *Proceedings of the ASME Int. Gas Turbine Conference and Exhibit*, Dusseldorf, Vol.4: Heat Transfer; Electric Power, 86-GT-132.
- Sivasegaram, S., and Whitelaw, J., 1969, Film cooling slots: the importance of lip thickness and injection angle, *J. Mechanical Engineering Science*, Vol.11, No.1, pp.22-27.
- Taslim, M., Spring, S., Mehlman, B., 1992, Experimental Investigation of Film Cooling Effectiveness for Slots of Various Exit Geometries, *J. of Thermo- physics and Heat Transfer*, Vol.6, No.2, pp.302-307.
- Uzol, O., and Camci, C., 2005, Heat Transfer, Pressure Loss and Flow Field Measurements Downstream of Staggered Two-Row Circular and Elliptical Pin Fin Arrays, *J. of Heat Transfer*, 127, No.5, pp.458-471.
- Wang F., Zhang J., Wang S., 2012, Investigation on Flow and Heat Transfer Characteristics in Rectangular Channel With Drop-Shaped Pin Fins, *Propulsion and Power Research*, Vol.1(1), pp.64-70.



Tuğba TUNÇEL received her B.Sc. degree from the Aerospace Engineering Department, METU, in 2015. She started her M.Sc. education in 2015 at the same department where she is also working as a graduate research assistant. Her research focuses on turbine aerodynamics and Computational Fluid Dynamics.



Harika S. KAHVECİ is an Assistant Professor at the Aerospace Engineering Department at METU, Turkey. She received her Ph.D in Mechanical Engineering from The Ohio State University in 2010, her M.S. degree in Aerospace Engineering from Penn State University in 2004, and her B.S. degree in 2002 from the same department of METU where she is currently teaching. She worked at General Electric Company for 11 years undertaking various responsibilities and worked on the design of aerodynamics, heat transfer and blade cooling of gas turbines. She is the recipient of the UTSR Gas Turbine Industrial Fellowship Award (2003), the Critical Difference for Women Fellowship (2008), and the ASME Best Technical Paper Award (2013), and received several company awards at GE. She was awarded the ASME Gas Turbine Award in 2015. Her research interests include design of gas turbines, engine aerothermodynamics and cooling systems, computational fluid dynamics and experimental techniques.